

Supporting Information for

P-doped NiMoO₄ Parallel Arrays Anchored on Cobalt Carbonate Hydroxide with Oxygen Vacancies and Mass Transfer Channels for Supercapacitor and Oxygen Evolution

*Feifei Wang,^a Kui Ma,^a Wen Tian,^a Juncai Dong,^b Han Han,^a Huipu Wang,^a Kuan Deng,^a Hairong Yue,^a Yu Xin Zhang,^c Wei Jiang^a and Junyi Ji^{*a, d}*

^a *School of Chemical Engineering, Sichuan University, Chengdu 610065, P. R. China*

^b *Beijing Synchrotron Radiation Facility, Institute of High Energy Physics, Chinese Academy of Sciences, Beijing 100049, P. R. China*

^c *College of Material Science and Engineering, Chongqing University, Chongqing, 400044, P. R. China*

^d *State Key Laboratory of Polymer Materials Engineering, Sichuan University, Chengdu 610065, P. R. China*

* Corresponding author.

Junyi Ji, E-mail: junyiji@scu.edu

Experimental Section

Synthesis of CoCH/CC:

All the raw materials purchased from Aladdin Co. were used directly without any further purification. The carbon cloth (2 cm×2 cm, WOS 1009, CeTech Co. Ltd, China) was first soaked with ethanol and DI water under sonication to eliminate the impurities, and then pretreated in 0.5 M KMnO₄ for 0.5 h to provide the growth seed crystal. In a typical process, Co(NO₃)₂·6H₂O (0.582 g), NH₄F (0.148 g) and urea (0.600 g) were dissolved in 35 mL deionized water with vigorous mixing for 15 min. Then the pink solution and the treated carbon cloth were directly transferred into a 50 mL autoclave and kept at 110 °C for 6 h. After cooling down to room temperature, the obtained Co(CO₃)_{0.5}OH·0.11H₂O/CC (CoCH/CC) was washed thoroughly with deionized water and ethanol for several times, and then dried at 60 °C.

Preparation of NiMoO₄@CoCH/CC

The preparation of NiMoO₄ parallel nanosheets anchored on the CoCH/CC nanowire arrays was achieved through hydrothermal reaction and the followed calcination treatment. Briefly, 0.150 g NaMoO₄·2H₂O, 0.180 Ni(NO₃)₂·6H₂O and 0.400 g thiourea were all added into 80 mL deionized water with vigorous stirring for 30 min. Then the mixture and the as-prepared CoCH/CC were transferred into a 50 mL autoclave and maintained at 180 °C for 15 h. After cooling down naturally, the obtained precursors were washed with deionized water and ethanol, and dried in vacuum at 60 °C overnight. To gain the NiMoO₄@CoCH/CC samples, the precursors were then calcinated at 300 °C in Ar atmosphere for 1 h. The contrast experiments were conducted as

aforementioned processes, but with the reaction time about 10 min, 30 min, 1 h and 10 h, respectively.

Preparation of NiMoP@CoCH/CC

To prepare the NiMoP@CoCH/CC samples, the NiMoO₄@CoCH/CC precursor and 30, 60 and 90 mg NaH₂PO₂ were placed into quartz boats respectively, and NaH₂PO₂ was placed at the upstream side of the NiMoO₄@CoCH/CC. Subsequently, the samples were heated at 300 °C for 1 h at a ramping rate of 2 °C min⁻¹ in 50 sccm Ar atmosphere, and then cooled naturally. The samples were labelled as NiMoP@CoCH/CC-n (n= 1, 2, 3), respectively. The weight of the active materials were recorded before and after the reaction (**Table S2**).

Material characterization

The scanning electron microscope (SEM, JEOL JSM-7610F), energy dispersive X-ray spectroscopy (EDS) and transmission electron microscopy (TEM, FEI Tecnai G20) were carried out to characterize the morphology and structure. The phase and valence states of the composites were identified by X-ray diffraction (XRD, Cu K α radiation) and X-ray photoelectron spectroscopy (XPS, PHI5000 Versa spectrometer) tests, respectively. The Raman measurements were performed using a DXRxi spectrometer (Thermo, 780 nm). X-ray absorption near-edge structure (XANES) and extended X-ray absorption fine structure (EXAFS) measurements were performed at 1W1B beamline of Beijing Synchrotron Radiation Facility (BSRF). The X-ray absorption spectra were detected in the transmission mode. Using the Athena program of the IFEFFIT package, the background of the spectra was removed by extrapolating the pre-edge region onto

the EXAFS region, and the $\chi(E)$ data were normalized with respect to the edge jump step. Then the normalized $\chi(E)$ was transformed from energy space to k -space with $\chi(k)$ multiplied by k^3 to compensate for the contributions from light scatters. Finally, the $k^3\chi(k)$ data in k -space ranging from 3.0 to 10.0 \AA^{-1} were Fourier-transformed to R -space to get the radial structure function spectra (RSFs). The XANES spectra of Ni foil and NiO were employed as the references.

Methods for RSFs simulation

The $\chi(k)$ data of the processed EXAFS spectra were fitted in R space ranging from 1.0 to 2.0 \AA with the Artemis program of the IFEFFIT package. From this simulation, structural parameters including coordination number (N), coordination distance (R), Debye-Waller factors (σ^2) and inner potential correction (ΔE_0) were obtained. Theoretical RSFs of the samples were calculated using FEFF and their crystal structure parameters searched in FindIt database were compiled as the input data.

Electrochemical measurement

Supercapacitor Test: All of the electrochemical measurements were studied with a three-electrode system (1 M KOH aqueous solution as the electrolyte). The NiMoP@CoOH/CC, Pt plate and Ag/AgCl electrode were employed as working electrode, counter electrode and reference electrode, respectively. Both the cyclic voltammetry (CV) and galvanostatic charge/discharge (GCD) tests were conducted on an electrochemical workstation (METROHM AUTOLAB M204) with a fixed potential window of -0.05 to 0.45 V at different scan rate. Electrochemical impedance spectroscopy (EIS) tests were conducted in the frequency arranging from 100 kHz to

0.01 Hz. The capacitive contribution can be further calculated by separating the current response i at a fixed potential V into capacitive effect ($k_1\nu$) and diffusion-controlled reaction ($k_2\nu^{1/2}$), according to Dunn: $i(V) = k_1\nu + k_2\nu^{1/2}$, where ν is the scan rate. By determining the k_1 and k_2 constants, the quantified analysis can be conducted. The specific capacitance is calculated according to the following equation: $C_s = It/S \cdot \Delta V$, where the I/S is the current density (mA cm^{-2}), t means the discharge time (t) and ΔV is the potential window (V). The square resistance of all samples were determined by the 4-probe measurement (Guangzhou four-probe technology Co., RTS-8). The NiMoP@CoCH/CC-2//a-MEGO asymmetric supercapacitor (ASC) was fabricated with NiMoP@CoCH/CC-2 as the positive electrode and the a-MEGO mixed with 10% PTFE as negative electrode. The mass of the active materials of the both electrode has to follow the formula: $m^+/m^- = C^-V^-/C^+V^+$, where the C^- is the specific capacitance, and V is the potential window of positive (+) and negative (-) electrodes, respectively. The energy density and power density were calculated by the formulae: $E = 0.5CV^2$ and $P = E/t$, respectively, where V is the working potential, t stands for the discharge time and C_s is the specific capacitance of the ASC.

Electrocatalytic tests: The electrocatalytic performance of the as-prepared composites were performed in the three-electrode device with 1 M KOH as electrolyte ($\text{pH} = 14$). The as-prepared samples, carbon rods and Ag/AgCl electrodes were used as working electrode, counter electrode and reference electrode, respectively. The LSV curves were tested at 5 mV s^{-1} and then corrected for iR . All potentials are referred to as RHE using the following equation: $E (\text{RHE}) = E (\text{Ag/AgCl}) + 0.059 \times \text{pH} + 0.097$.

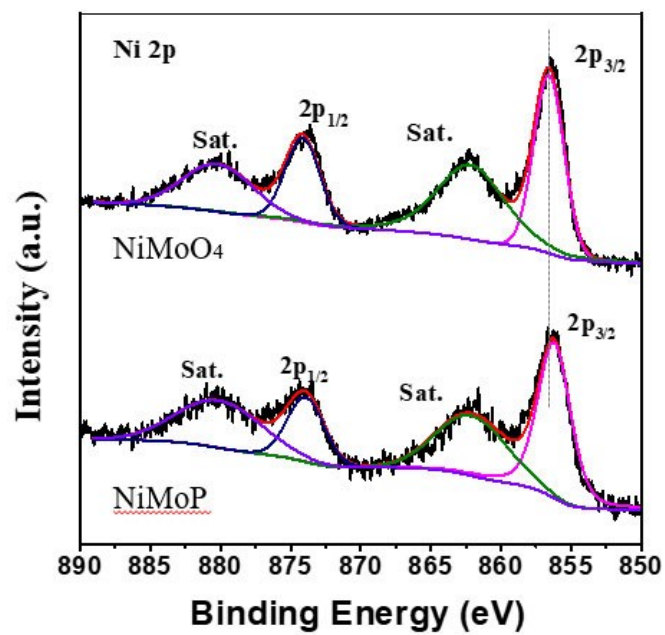


Figure S1. Comparison of the Ni 2p spectrum of the NiMoO₄@CoCH precursor and the NiMoP@CoCH.

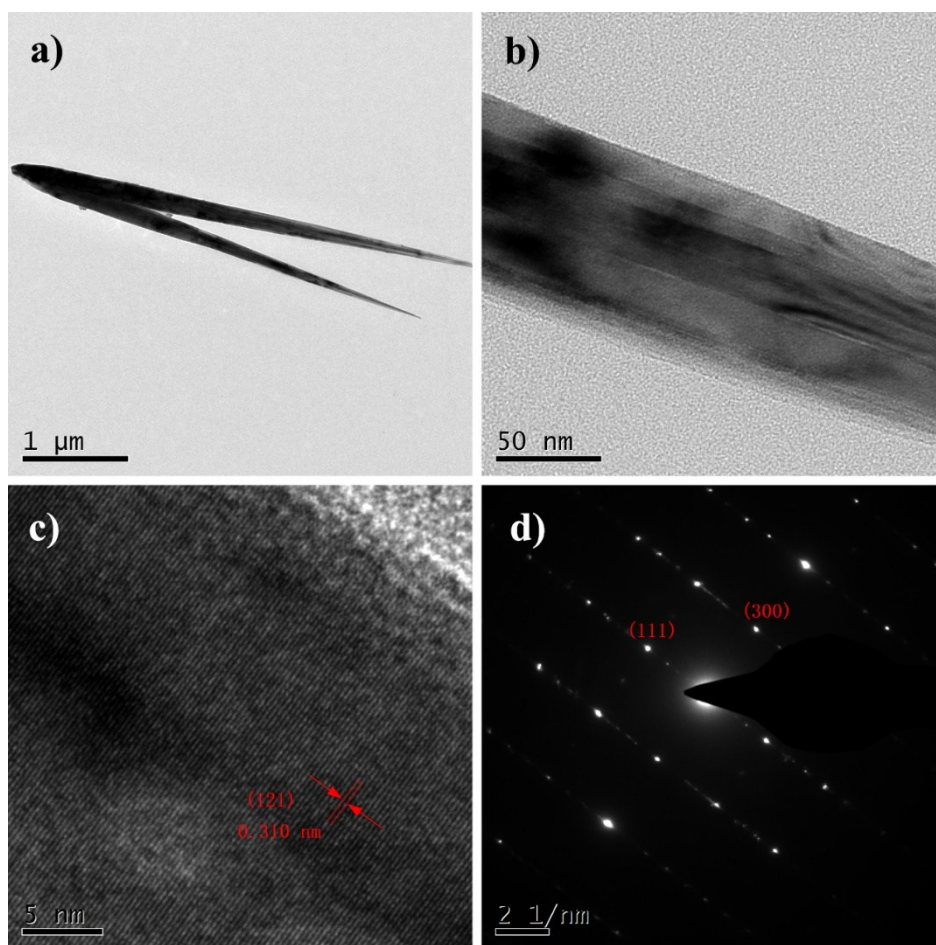


Figure S2 a) TEM images of the CoCH composite, b) the high-resolution image, c) the crystalline of CoCH and d) the SAED pattern.

Figure S2a, b) show the low and high resolution TEM images of the CoCH nanowire arrays, respectively. As can be seen, the length of the CoCH wire is round 4~5 μm , which can be better for growth of the secondary structure. The lattice fringes show an interplanar spacing of around 0.310 nm, which can be ascribed to the (121) planes of the CoCH phase (**Figure S2c**). **Figure S2d** exhibits the SEAD pattern of CoCH with the diffraction spots, demonstrating the single crystal structure of the CoCH composite. Specifically, the two spots can be indexed to (111) and (300) planes of CoCH phase.

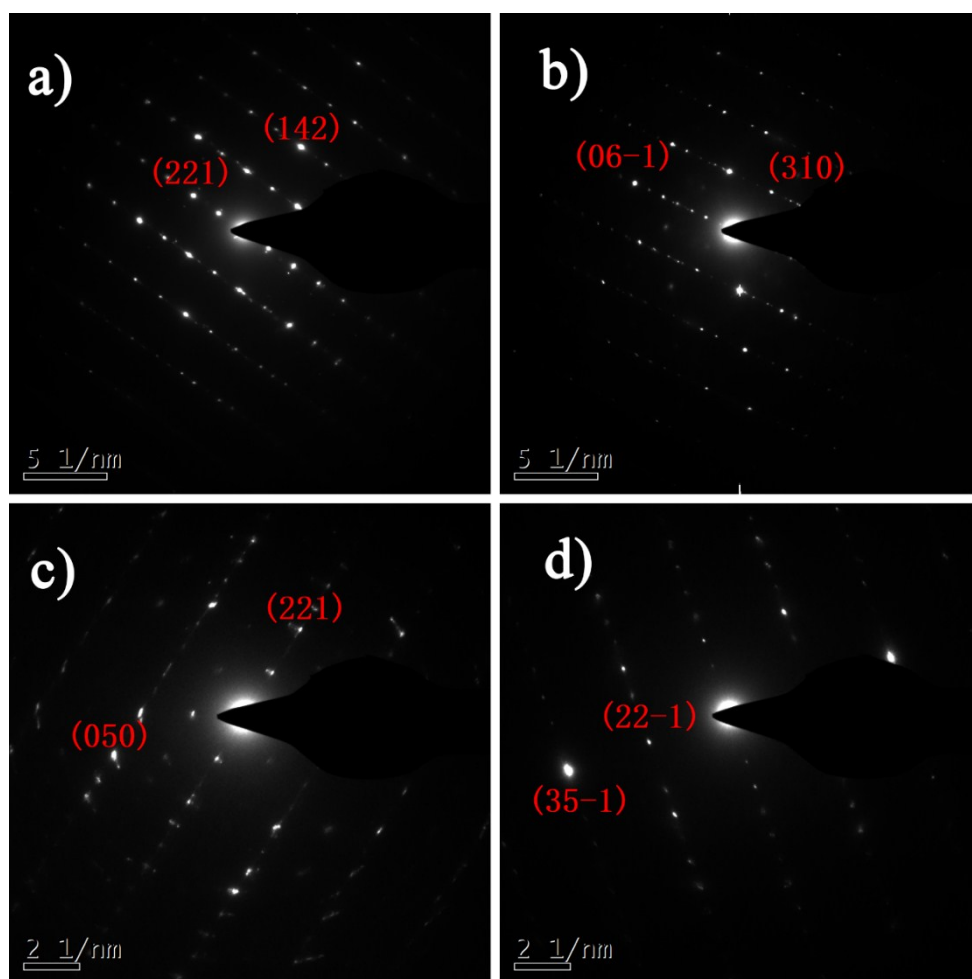


Figure S3 SAED images of $\text{NiMoO}_4@\text{CoCH}/\text{CC}$ after reaction for a), b) 10 min and c), d) 30 min.

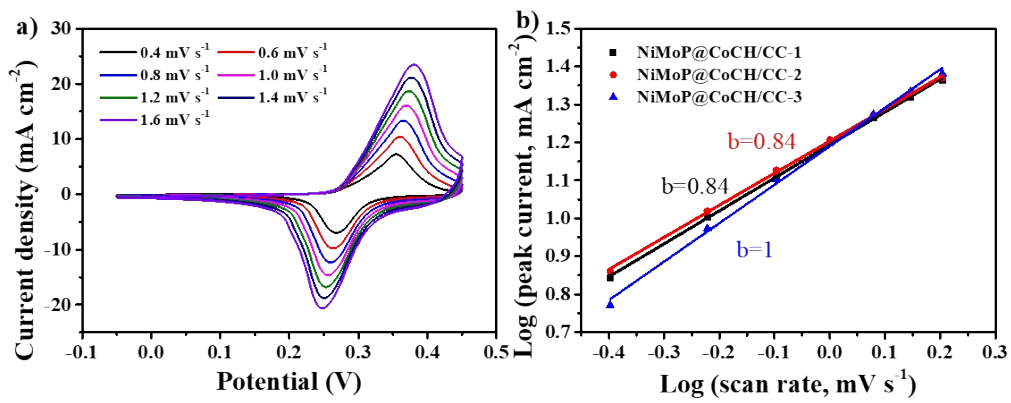


Figure S4 a) CV curves from 0.4 to 1.6 mV s⁻¹, b) b values calculated from peak anodic current density.

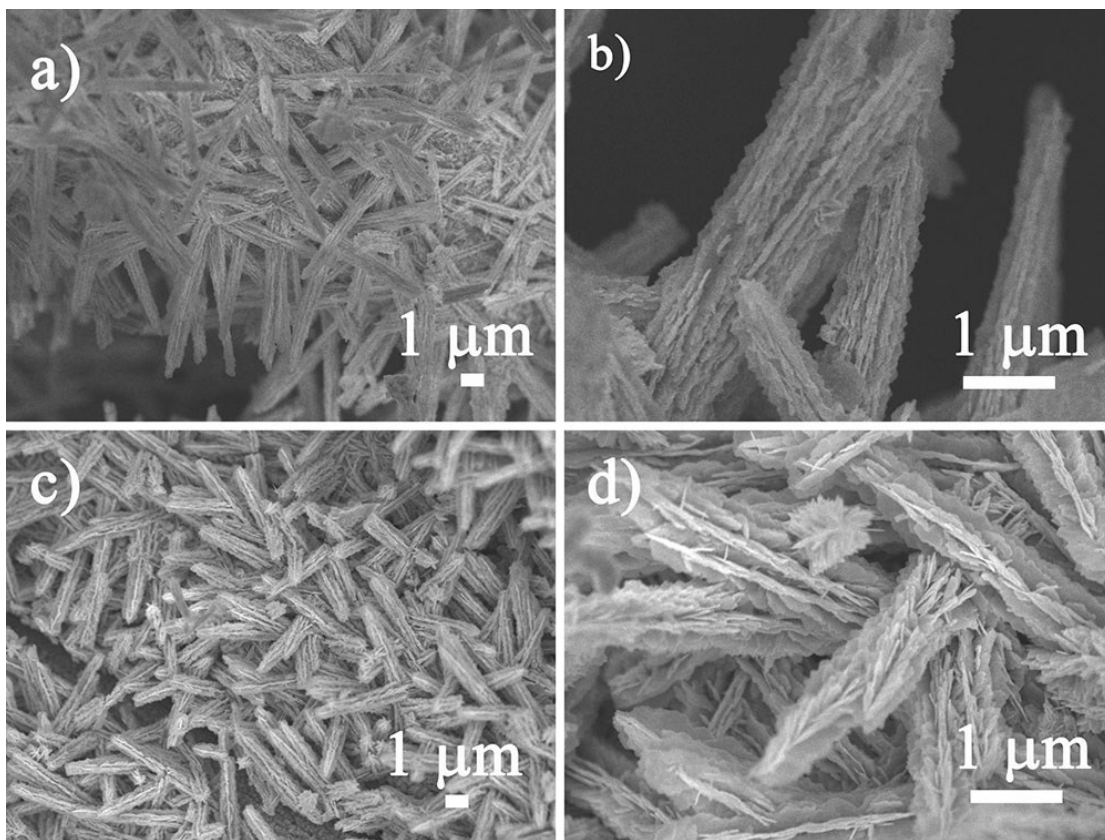


Figure S5 a) SEM images of a) and b) of the NiMoP@CoCH/CC composites after long cycling test.

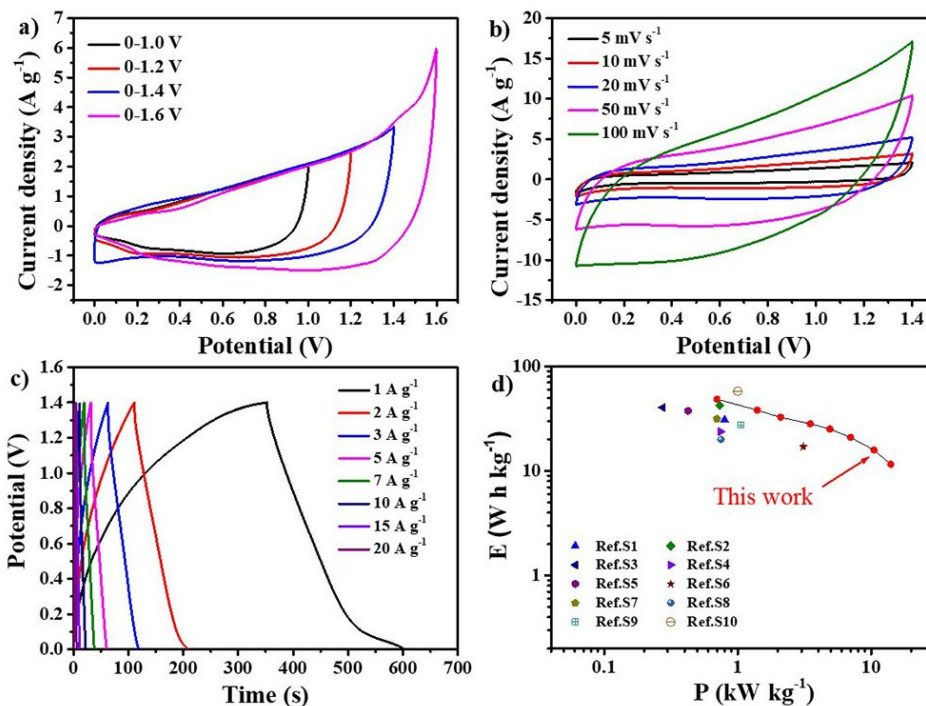


Figure S6 a) CV at 10 mV s^{-1} with different potential windows, b) CV at the scan rate from 5 to 100 mV s^{-1} , c) Charge-discharge curves of NiMoP@CoCH/CC-2 //a-MEGO ASCs. d) Ragone plots of the as-prepared ASCs.

To evaluate the practical application capability of the as-prepared composite, the ASCs are assembled with the NiMoP@CoCH/CC-2 and a-MEGO as the positive and negative electrodes, respectively. The operating potential of the ASCs can be broadened due to the different operation potential windows of the two electrodes. To estimate the best operation potential windows, a series of CV measurements with different operation potential are tested (**Figure S5a**). With the increment of the operation voltage, the redox region of the ASCs is enlarged gradually until an apparent polarization occurs at 1.6 V . Thus the operation of 1.4 V is selected to further discuss the energy storage performance. **Figure S5b** shows the CV curves at different scan rate ranging from 5 to 100 mV s^{-1} in 1 M KOH solution. The response current increases apparently with the increment of the scan rate, which is in line with the three-electrode CV results. The GCD plots at various current densities are also plotted in **Figure S5c**. The energy densities and power densities are the two critical parameters to assess the performance of ASCs in practical application. The Ragone plots of the NiMoP@CoCH/CC-2//a-MEGO-ASCs device are listed in **Figure S5d**. A highest energy density of 48.6 Wh h

kg⁻¹ (with power density of 700 W kg⁻¹) and highest power density of 14.0 kW kg⁻¹ (with energy density of 11.9 W h kg⁻¹) can be achieved, respectively, which are comparable or better than most of the previously reported high-end supercapacitor electrodes.^{S1-S10}

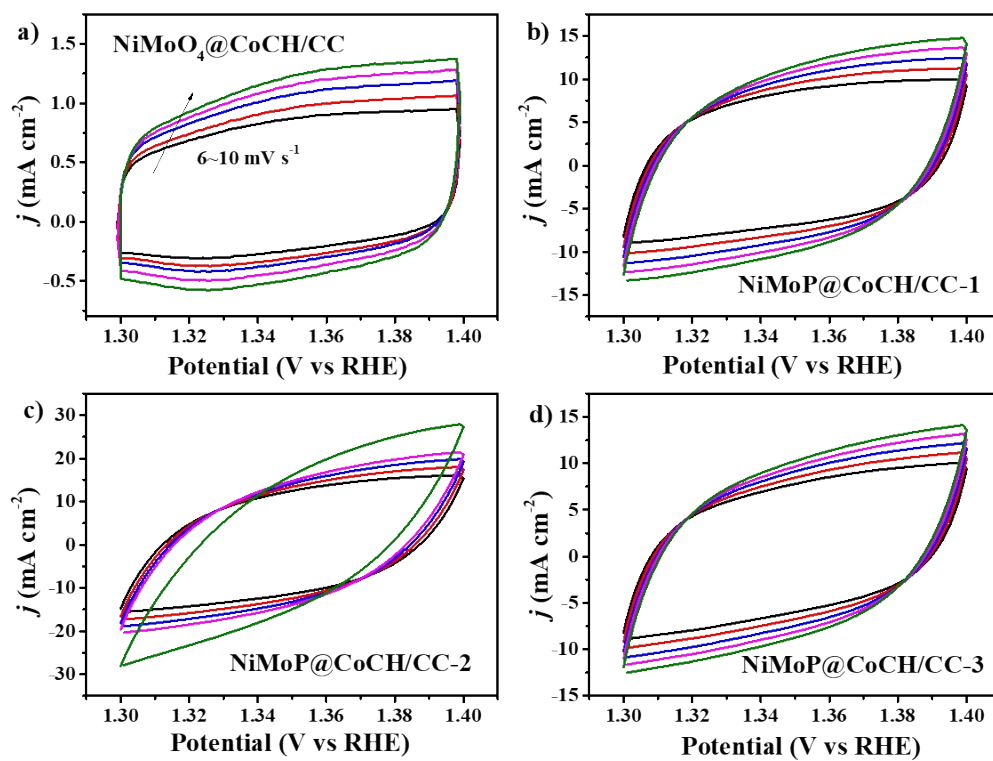


Figure S7 CV curves of a) NiMoO₄@CoCH/CC, b) NiMoP@CoCH/CC-1 c) NiMoP@CoCH/CC-2 and NiMoP@CoCH/CC-3 at different scan rates from 6 to 10 mV s⁻¹.

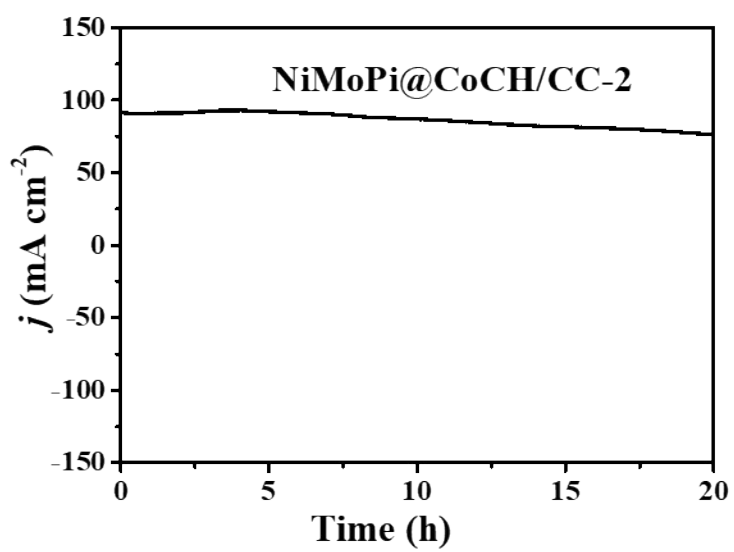


Figure S8. Long-term stability of NiMoP@CoCH/CC-2.

Table S1. Local structural parameters in the first Ni-O shell extracted from Ni *K*-edge EXAFS curve-fitting for NiMoO₄@CoCH/CC and NiMoP@CoCH/CC.

Sample	Shell	N^a	R (Å) ^b	σ^2 (10 ⁻³ Å ²) ^c	ΔE_0 (eV) ^d	<i>R</i> -factor
NiMoO ₄ @CoCH/CC	Ni-O	5.8	2.117	3.0	2.976	0.005
NiMoP@CoCH/CC	Ni-O (1) ^e	4.2	2.070	6.3	0.367	0.015
	Ni-O (2) ^f	6.0	2.315	3.5	5.023	0.015

^a Coordination number; ^b Distance between absorber and backscatter atoms; ^c Debye-Waller factor; ^d Inner potential correction. ^e Ni-O path in the NiMoO₄. ^f Ni-O path in the Ni₃(PO₄)₂. Errors: *N*, ± 10%; *R*, ± 0.01 Å.

Table S2. The mass density of the active materials of CoCH, NiMoO₄@CoCH and NiMoP@CoCH anchored on the carbon cloth.

Composites	Mass (mg cm⁻²)^a
CoCH	1.90
NiMoO₄@CoCH	3.25
NiMoP@CoCH	3.50

^a The actual mass error of the composites loaded on the carbon cloth is around $\pm 10\%$.

Table S3. The mass ratio of different elements in the NiMoP@CoCH/CC-n (n= 1, 2, 3) calculated from the EDS results.

Elements (wt.%) Samples	Ni	Mo	O	Co	C	P
NiMoP@CoCH-1	27.5	20.3	22.9	13.3	10.2	5.8
NiMoP@CoCH-2	27.2	18.3	19.1	11.4	19.1	7.1
NiMoP@CoCH-3	25.2	20.1	18.5	14.3	18.5	9.8

Table S4. Areal and specific capacitance of the NiMoP@CoCH/CC electrode compared with the transition metal-based electrodes previously reported in literatures.

Electrode materials	Electrolyte	Areal capacitance	Specific capacitance	References
NiMoP@CoCH/CC	1 M KOH	4.00 F cm ⁻² (1 mA cm ⁻²)	1143 F g ⁻¹	This work
Ni _x Co _{1-x} P	2 M KOH	-	548 F g ⁻¹	Ref.S11
NiCoP/NiCo-OH/CC	1 M KOH	-	1100 F g ⁻¹	Ref.S12
ZnCo ₂ O ₄ @NiMoO ₄ ·H ₂ O	1 M KOH	3.53 F cm ⁻² (1 mA cm ⁻²)	-	Ref.S13
NiMoO ₄ /NF	2 M KOH	3.50 F cm ⁻² (5 mA cm ⁻²)	-	Ref.S14
Co ₂ P	6 M KOH	-	412.7 F g ⁻¹	Ref.S15
Co(P, S)	6 M KOH	2.01 F cm ⁻² (3.3 mA cm ⁻²)	-	Ref.S16
NiMoO ₄ /NF	2 M KOH	-	1091 F g ⁻¹	Ref.S17
Co ₃ O ₄ @CoMoO ₄	3 M KOH	-	1040 F g ⁻¹	Ref.S18
NiCoP@NF	6 M KOH	0.857 F cm ⁻² (1 mA cm ⁻²)	-	Ref.S19
Ni _x P@NF	6 M KOH	1.684 F cm ⁻² (2 mA cm ⁻²)	-	Ref.S20

Table S5. 4-probe measurement of the resistance and conductivity of the NiMoO₄@CoCH/CC and NiMoP@CoCH/CC-n (n=1, 2, 3).

Sample	Resistance ($\Omega \cdot \text{cm}$)	Conductivity (S/cm)
NiMoO ₄ @CoCH/CC	0.049 \pm 0.003	20.62 \pm 1.39
NiMoP@CoCH/CC-1	0.028 \pm 0.004	35.34 \pm 4.09
NiMoP@CoCH/CC-2	0.017 \pm 0.001	59.43 \pm 2.30
NiMoP@CoCH/CC-3	0.066 \pm 0.005	15.23 \pm 1.16

Table S6. Electrocatalytic performance of NiMoP@CoCH/CC electrode compared with the transition metal-based electrodes previously reported in literatures.

Electrocatalyst	Electrolyte	Overpotential	Tafel	References
NiMoP@CoCH/CC	1 M KOH	267 mV (40 mA cm ⁻²)	99 mV dec ⁻¹	This work
Mn-Co-P@MnCo ₂ O ₄	1 M KOH	269 mV (10 mA cm ⁻²)	102 mV dec ⁻¹	Ref.S21
Ni ₂ P	1 M KOH	420 mV (10 mA cm ⁻²)	128 mV dec ⁻¹	Ref.S22
Co ₃ O ₄ @Ni ₃ S ₂ /NF	1 M KOH	260 mV (20 mA cm ⁻²)	121.7 mV dec ⁻¹	Ref.S23
GDY@NiFe	1 M KOH	260 mV (10 mA cm ⁻²)	95 mV dec ⁻¹	Ref.S24
Ni-CoP@C	1 M KOH	279 mV (10 mA cm ⁻²)	54 mV dec ⁻¹	Ref.S25
Ni _{0.9} Fe _{0.1} PS ₃	1 M KOH	329 mV (20 mA cm ⁻²)	69 mV dec ⁻¹	Ref.S26

Reference

- S1. Y. Liu, G. Liu, X. Nie, A. Pan, S. Liang and T. Z. H. U., *J. Mater. Chem. A*, 2019, 7, 11044-11052.
- S2. P. Sivakumar, J. Milan, J. Min Gyu, G. Aharon and P. Ho Seok, *J. Mater. Chem. A*, 2019, 7, 11362-11369.
- S3. S. J. Zhu, L. Li, J. B. Liu, H. T. Wang, T. Wang, Y. X. Zhang, L. Zhang, R. S. Ruoff and F. Dong, *ACS Nano*, 2018, 12, 1033-1042.
- S4. D. Zhao, H. Liu and X. Wu, *Nano Energy*, 2018, 57, 363-370.
- S5. X. Zhang, L. Wei and X. Guo, *Chem. Eng. J.*, 2018, 353, 615-625.
- S6. P. Yang, Z. Wu, Y. Jiang, Z. Pan, W. Tian, L. Jiang and L. Hu, *Adv. Energy Mater.*, 2018, 8, 1801392.
- S7. Y. Xu, S. Hou, G. Yang, X. Wang, T. Lu and L. Pan, *Electrochim. Acta*, 2018, 285, 192-201.
- S8. W. Wang, N. Zhang, Z. Shi, Z. Ye, Q. Gao, M. Zhi and Z. Hong, *Chem. Eng. J.*, 2018, 338, 55-61.
- S9. H. Sk. Khaja and Y. Jae Su, *Chem. Eng. J.*, 2018, 361, 1030-1042.
- S10. S. Sun, J. Luo, Y. Qian, Y. Jin, Y. Liu, Y. Qiu, X. Li, C. Fang, J. Han and Y. Huang, *Adv. Energy Mater.*, 2018, 8, 1801080.
- S11. Y. Xu, S. Hou, G. Yang, X. Wang, T. Lu and L. Pan, *Electrochim. Acta*, 2018, 285, 192-201.
- S12. X. Li, H. Wu, A. M. Elshahawy, L. Wang, S. J. Pennycook, C. Guan and J. Wang, *Adv. Funct. Mater.*, 2018, 28, 180036.
- S13. C. Chen, S. Wang, X. Luo, W. Gao, G. Huang, Y. Zeng and Z. Zhu, *J. Power Sources*, 2018, 409, 112-122.
- S14. Z. Wang, G. Wei, K. Du, X. Zhao, M. Liu, S. Wang, Y. Zhou, C. An and J. Zhang, *ACS Sustainable Chem. Eng.*, 2017, 5, 5964-5971.
- S15. M. Cheng, H. Fan, Y. Xu, R. Wang and X. Zhang, *Nanoscale*, 2017, 9, 14162-14171
- S16. A. M. Elshahawy, C. Guan, X. Li, H. Zhang, Y. Hu, H. Wu, S. J. Pennycook and J. Wang, *Nano Energy*, 2017, 39, 162-171.

- S17. S. Peng, L. Li, H. B. Wu, S. Madhavi and X. W. Lou, *Adv. Energy Mater.*, 2015, 5, 1401172.
- S18. Z. Gu, R. Wang, H. Nan, B. Geng and X. Zhang, *J. Mater. Chem. A*, 2015, 3, 14578-14584.
- S19. Y. Lan, H. Zhao, Y. Zong, X. Li, Y. Sun, J. Feng, Y. Wang, X. Zheng and Y. Du, *Nanoscale*, 2018, 10, 11775-11781.
- S20. X. Cao, D. Jia, D. Li, L. Cui and J. Liu, *Chem. Eng. J.*, 2018, 348, 310-318.
- S21. J. Han, S. Hao, Z. Liu, A. M. Asiri, X. Sun and Y. Xu, *Chem. Commun.*, 2017, 54, 1077-1080.
- S22. B. Qiu, L. Cai, Y. Wang, Z. Lin, Y. Zuo, M. Wang and Y. Chai, *Adv. Funct. Mater.*, 2018, 28, 1706008.
- S23. Y. Gong, Z. Xu, H. Pan, Y. Lin, Z. Yang and X. Du, *J. Mater. Chem. A*, 2018, 6, 5098-5106.
- S24. G. Shi, C. Yu, Z. Fan, J. Li and M. Yuan, *ACS Appl. Mater. Interface*, 2018, 11, 2662-2669.
- S25. X. Han, C. Yu, H. Huang, W. Guo, C. Zhao, H. Huang, S. Li, Z. Liu, X. Tan, Z. Gao, J. Yu and J. Qiu, *Nano Energy*, 2019, 62, 136-143.
- S26. P. Li and H. C. Zeng, *J. Mater. Chem. A*, 2018, 54, 1077-1080.